Cyclic Nanoindentation and Finite Element Analysis of Ti/TiN and CrN Nanocoatings on Zr-Based Metallic Glasses Mechanical Performance

Aymen Tekaya, Hamza Ghulman, Tarak Benameur, Sid Labdi

Cyclic Nanoindentation and Finite Element Analysis of Ti/TiN and CrN Nanocoatings on Zr-Based Metallic Glasses Mechanical Performance

A. Tekaya, H.A. Ghulman, T. Benameur, and S. Labdi

Cyclic depth-sensing nanoindentation tests are carried out to unravel the effect of monolithic and multilayer thin coatings on load-bearing capacity and stress distribution in the coating-Zr-based metallic glass systems. Thin films of TiN, CrN, and Ti/TiN multilayer, having thickness of 300 nm, are deposited on $Zr_{60}Ni_{10}Cu_{20}Al_{10}$ and $Zr_{50}Cu_{40}Al_{10}$ metallic glasses by RF sputtering technique. Strain softening occurs over several cycles in Zr-based metallic glasses, CrN, and TiN films as evidenced by a disparity between the unloading and reloading sequences. However, the cyclic nanoindentation of Ti/TiN multilayer coating results in a hysteresis loop in the load-depth profiles, and this event depends on the number of cycles and the loading rates. AFM and SEM characterization of remnant imprints revealed microcraks and crack-like shear bands in nanocoatings and Zr-based metallic glasses, respectively. Based on shear-fracture driven plastic flow of the coatings, a modified cavity model is used to determine the shear stress evolution as a function of penetration depth. The finite-element simulations predicted the stress distribution beneath the indenter and are well consistent with the evolving trend of shear stress obtained from experiments.

Keywords cyclic nanoindentation, modeling and simulation, nanocoatings, Zr-based metallic glasses

1. Introduction

The development of bulk metallic glasses (BMGs) with remarkable combination of properties, compared with their crystalline counterparts, such as high strength up to 5 GPa and large elastic limit that can reach 2% has prompted interests in their potential as structural materials (Ref 1). They possess a number of remarkable functional and structural properties. While some properties, for example, thermal conductivity, expansion, and specific heat, are not unusual, the corrosion resistance and low temperature dependence of resistivity are potentially attractive (Ref 2). However, the plastic deformation of these alloys below the transition temperature (T_g) is characterized by strain localization in shear bands (Ref 3). The work-softening in the bands leads to nearly zero ductility in tension, but this can be palliated by a dispersion of a second phase to disrupt shear band propagation (Ref 4). Moreover, much current research was directed at improving their mechanical performance by mechanical treatments, such as cold rolling which induces an important increase of plasticity. It has been mostly attributed to the development of an inhomogeneous microstructure consisting of soft and hard regions. The soft regions are preferred locations on subsequent loading of new shear bands. The hard regions inhibit catastrophic propagation and force the branching and multiplication of shear bands (Ref 5, 6). Surface treatment was also applied such as the introduction of compressive residual stresses through shot peening (Ref 7, 8) Additionally, thin films deposited on polycrystalline alloys are widely recognized for their beneficial effects, ranging from protective coatings on mechanical tools, increased fatigue resistance, to the diffusion barrier in microelectronic industry (Ref 9, 10). Attention has therefore been focused on the influence of coatings on the BMG's mechanical behavior and functional properties. It was found that copper films inhibited the rapid propagation of primary shear bands, and promoted the multiplication of shear bands in $Zr_{41}Ti_{14}Cu_{12.5}Ni_{10}Be_{22.5}$ substrates, which led to larger plastic strain in compression (Ref 11). Qin et al. (Ref 12, 13) have showed that Ti coating can improve the corrosion resistance and mainly hydroxyapatite forming ability of Zr-based bulk metallic glass for biomedical applications. Nevertheless, few studies have been devoted to elucidate the effect of thin coatings on the mechanical performance of bulk metallic glasses. In previous work, the results of an optimization in the design of monolithic TiN and Ti/TiN multilayer-coated Zr-based metallic glasses, as well as quantitative tribological analyses, have been reported (Ref 14, 15). The importance of an alternation of ductile and hard thin layers with an optimized nanoscaled thickness on load-bearing capacity was explored and found that this greatly facilitated the accommodation of the stress between the layers and significantly reduces the shear stress at the film/substrate interface. This paper represents an expansion on our recent findings using cyclic nanoindentation. It is a variation to the conventional test, where the sample is reloaded immediately to even higher loads or depths than the previous loading cycle. It was used to study phase

A. Tekaya, Laboratoire de Génie Mécanique, LR99ES32, University of Monastir, ENIM, 5019 Monastir, Tunisia; **H.A. Ghulman**, Mechanical Engineering Department, Umm Al Qura University, CEIA, 21955 Makkah Mukarama, KSA; **T. Benameur**, Laboratoire de Génie Mécanique, LR99ES32, University of Monastir, ENIM, 5019 Monastir, Tunisia and Mechanical Engineering Department, Umm Al Qura University, CEIA, 21955 Makkah Mukarama, KSA; and **S. Labdi**, LAMBE, UMR8587, Université dEvry Val dEssonne, 91025 Evry Cedex, France. Contact e-mail: t.Benameur@enim.rnu.tn and ttbenameur@uqu.edu.sa.

transformations under stress and to probe sensitive dislocation-microstructure interactions (Ref 16). Indeed, the unloading-reloading paths do not necessarily overlap in crystalline alloys, resulting in strain hardening manifested as hysteresis loops in the load-depth curve or in strain softening (manifested as disparity in the load-depth curve) due to the dislocations generated beneath indenter (Ref 17). While metallic glasses are free of linear and bi-dimensional defects, disparities between unloading and reloading paths are found, and this event becomes more marked at higher loads. Moreover, finite element method (FEM) cyclic nanoindentation experiments are conducted to shed further light on the effect of the three type of coatings TiN and Ti/TiN multilayers on Zr-based metallic glass mechanical performance. Combining numerical nanoindentation simulation and experimental load-displacement data enables the determination of the variation of shear stress and plastic deformation distribution.

2. Experimental Details

Monolithic TiN and Ti-TiN multilayer nanocoatings were deposited on $Zr_{60}Ni_{10}Cu_{20}Al_{10}$ BMG substrate (Zr60_BMG), and CrN monolayer coating was deposited on $Zr_{50}Cu_{40}Al_{10}$ BMG (Zr50_BMG) using RF sputtering technique in nitrogen and argon atmosphere at room temperature. The targets used in the deposition process were 99.9% pure titanium and 99.9% pure chromium targets. The typical base pressure in the deposition chamber was about 1.33×10^{-6} Pa, and the total working pressure was 0.66 Pa. The parameters used for the TiN and CrN monolayer and Ti-TiN multilayer coatings are shown in Table 1. Typical deposition rates of about 3 nm/min for Ti and 0.9 nm/min for TiN were obtained. Ti-TiN multilayer coatings were elaborated with a period thickness $\Lambda = 5$ nm. The samples were cleaned with acetone and alcohol ultrasonic baths before the deposition process. The obtained coatings thickness is about 300 nm. The nanoindentation tests were performed using a Hysitron triboscope apparatus connected to a digital instrument D3100 atomic force microscopy running in STM mode. Before indentation measurements, the system was calibrated by conducting several indents on a fused silica sample under normal loads. Machine compliance, thermal drift, and area function were corrected as described in (Ref 18). The load and depth resolution of the nanoindenter were 1 nN and 0.04 nm, respectively. The hardness H and the reduced Young's modulus E_r were measured using a Berkovich tip with a total included angle of 142.3° and a radius of curvature of approximately 100 nm. Each test was repeated at least five times in order to evaluate the reproducibility of the data and determine the associated error values. In order to probe the mechanical behavior of the obtained systems at a micrometric level, indentations were also made using digital Vickers hardness machine with loads varying from 3 N to 10 N. The visualization of the relevant imprints of microindentation with scanning electron microscopy (SEM) was performed using a Zeiss Gemini DSM 982 microscope.

3. Results

3.1 Cyclic Nanoindentation Profiles and Images of a Contact Zone

Cyclic nanoindentation measurements were designed in order to clarify the operating deformation mechanisms and shear band formation at interfaces in nanocoatings/Zr-BMG systems subjected to loading cycles. In fact, the global shape of the P-h curve differs from one material to the next, and these variations usually are local perturbations (discontinuities) characteristic of energy-absorbing or energy-releasing events occurring beneath the indenter tip (Ref 19). The maximal normal load was gradually increased from 1000 to 6000 μN with six steps as illustrated in Fig. 1. The normal load is unloaded after each step to the pre-set minimal load. The hardness and reduced elastic modulus were evaluated from the obtained load-displacement curves at each step using the model of Oliver and Pharr (Ref 20).

Typical load-displacement plots of Zr60_BMG for incremental cyclic loadings at 500 and 1000 μN/s loading rates are shown in Fig. 2(a) and (b), respectively. The Insets of Fig. 2 illustrate the AFM images of residual impressions. One can notice that in the fourth cycle, the path of reloading curve does not follow completely the unloading curve of previous cycle. When sections of the curve containing the unloading-reloading paths are magnified, it becomes clear that they do not overlap but form an open jaw as seen inset of Fig. 2(a). Note that the disparity between the unloading and reloading paths increases with increasing applied load or indentation depth. Increasing the loading rate, the disparity is detected at the sixth cycle, as seen inset of Fig. 2(b).The open jaw signifies that the sample behavior was softer on reloading compared to the previous unloading path. Furthermore, the loading profiles exhibit a discrete displacement bursts, corresponding to a sudden penetration of the indenter in the material without increase of the applied load. This phenomenon named "pop-in" has been

Table 1 Details of deposition parameters of TiN, CrN monolayers and Ti/TiN multilayer coatings

Parameter	Value
Total pressure (Pa)	0.66
N_2 gas pressure (Pa)	0.07 (CrN,TiN) 0 (Ti)
Target-to-substrate distance (mm)	70
Pre-deposition vacuum (Pa)	1.10^{-6}
Temperature of substrate holder (°C)	35
Deposition time (min)	90
Sputtering power density (W/cm^2)	0.63
Auto-bias voltage (V)	−300

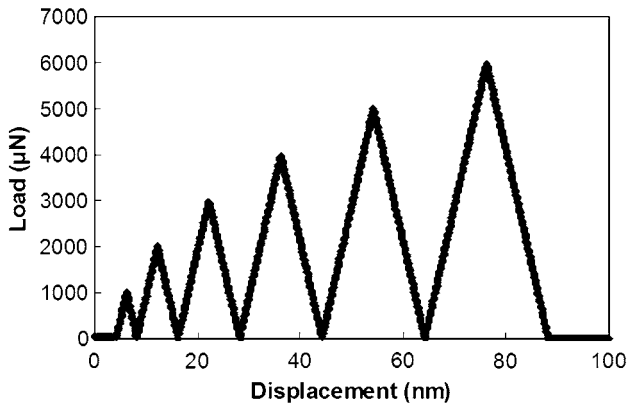

Fig. 1 Typical load vs. time function in cyclic nanoindentation tests (incremental cyclic loading) using Hysitron nanoindenter

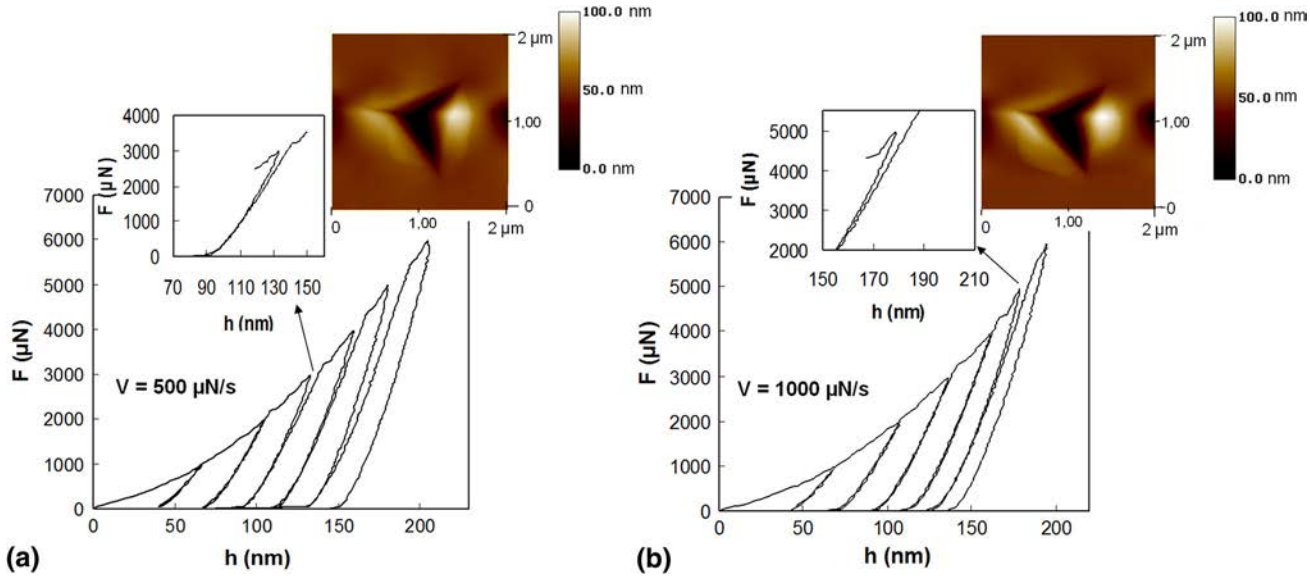

Fig. 2 Cyclic nanoindentation curves performed on $Zr_{60}Ni_{10}Cu_{20}Al_{10}$ at loading rates of (a) 500 µN/s and (b) 1000 µN/s

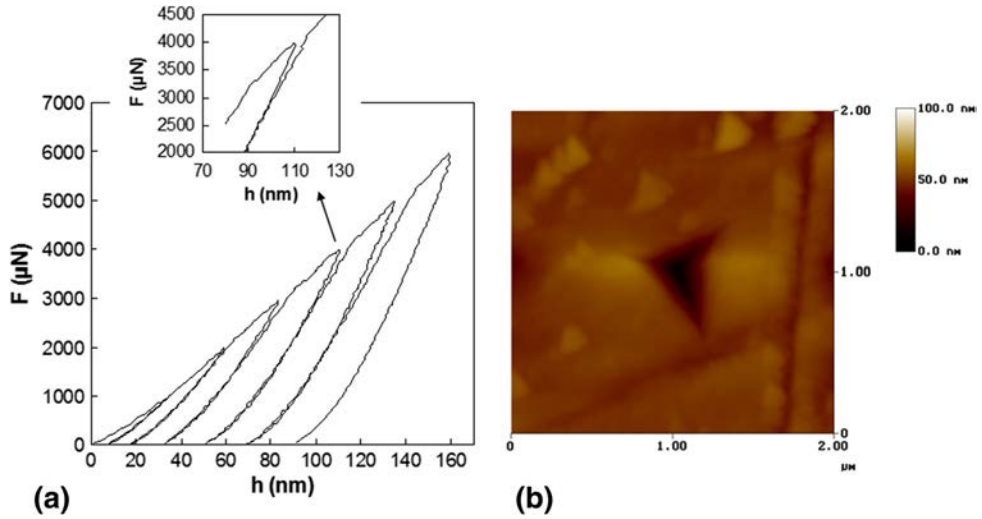

Fig. 3 (a) Cyclic nanoindentation curve performed on TiN coated $Zr_{60}Ni_{10}Cu_{20}Al_{10}$ at loading rate of 500 µN/s (b) AFM image of the obtained imprint after nanoindentation test

already reported in the literature and associated with a plastic flow consequence of the activation of individual shear bands underneath the indenter tip (Ref 21).

In fact, instead of dislocation motion, plastic deformation in metallic glasses at room temperature begins with the activation of shear transformation zones (STZs) in which clusters of atoms rearrange under an applied stress (Ref 22, 23) As the stress is increased, more STZs become active and connect to form shear bands in which the plastic strain is localized (Ref 24). The medium-range atomic order in the deformed matter (Ref 25) is altered by heavy deformation such as under indentation. As heavy deformation leads to creation of free volume (Ref 26) and to local heating, temperatures in shear bands have been shown to increase by hundreds of degrees (Ref 27). All of these effects lead to strain softening. However, a similar disparity event is observed at load above 3000 µN on monolithic TiN-coated Zr60-based BMG as shown in Fig. 3(a). Magnified unloading-reloading paths obtained and AFM image of residual impression after the cyclic tests are given in Fig. 3(a) and (b). Once again, note that the disparity events increase as the indentation load of cycling increases.

Unlike for both Zr60-based BMG and TiN/Zr60-based BMG system, hysteresis loops are produced in the case of Ti/TiN multilayer coating which signifies that materials' resistance to deformation becomes greater during reloading path comparing to the unloading path (Fig. 4a). These results are similar for all the tests performed, this proves that the obtained curves really reflect the material behavior and are not artifacts of the test procedure or equipment.

The load-displacement curve obtained using incremental cyclic nanoindentation performed on CrN-coated Zr50-based BMG at a loading rate of 500 µN/s is shown in Fig. 5(a). It is

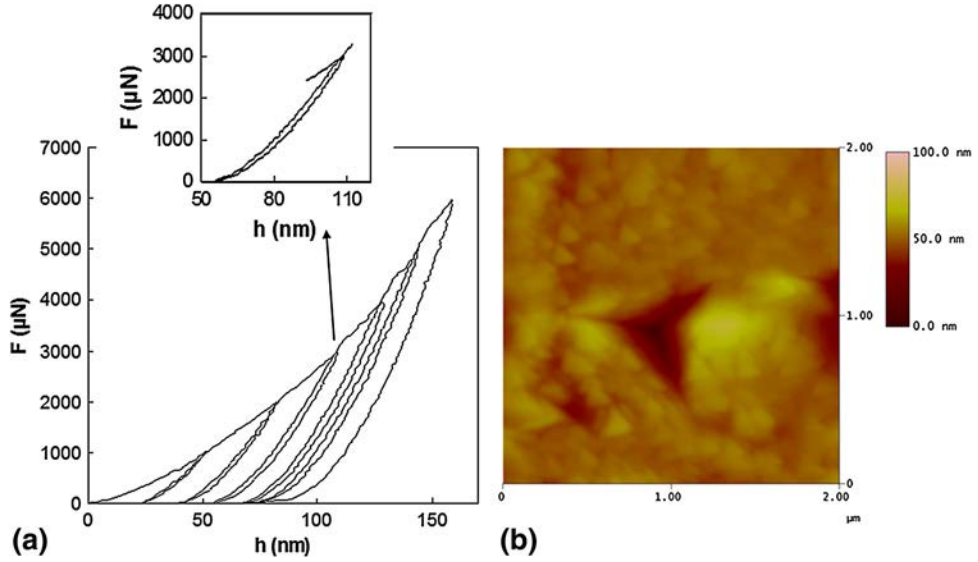

Fig. 4 (a) Cyclic nanoindentation curve performed on Ti/TiN coated $Zr_{60}Ni_{10}Cu_{20}Al_{10}$ at loading rate of 500 μN/s (b) AFM image of the obtained imprint after nanoindentation test

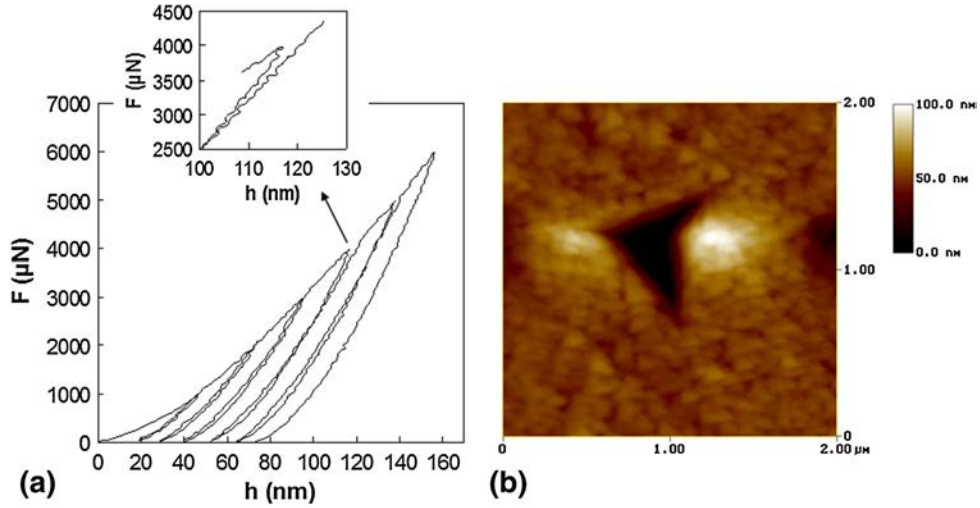

Fig. 5 (a) Cyclic nanoindentation curve performed on CrN coated $Zr_{50}Cu_{40}Al_{10}$ at loading rate of 500 μN/s (b) AFM image of the obtained imprint after nanoindentation test

worth noting that both hysteresis and disparity events are clearly illustrated. The hysteresis loop is seen at a load lower than 3000 μN. However, the disparity between unloading-reloading paths (inset in Fig. 5a) appears at higher loads or higher depths of penetration. The obtained residual imprint observed after the test is shown in Fig. 5(b). Evidence of greater localized plasticity of CrN films as indicated by the larger remnant indent is found compared to the TiN or Ti/TiN coatings. However, in order to probe the deformation modes at depths greater than the scale of the coating thickness and elucidate the shear band pattern beneath the indenter, Vickers indentation tests were performed at a range of loads from 2 to 10 N for the uncoated and coated Zr-based BMGs with TiN, CrN, and Ti/TiN films.

The corresponding deformation features inside the impressions are seen in Fig. 6. A different response of the operative deformation mechanisms under the indentation is found. Quantitative analysis of crack patterns and damage mechanism generated in the vicinity of the corner of pyramidal were detailed by Richter (Ref 28). Indeed, representative SEM micrographs of residual impressions on TiN-coated Zr60-based BMG, which illustrate characteristic types of damage are shown in Fig. 6(a) and (b). It can be seen that under 3 N applied load, TiN coating presents inner circumferential cracks with nearly constant spacing from each other (type III). In Fig. 6d, radial cracks which are not extensions of the indentation diagonal are found in the case of the CrN films (called ''claws''-type IV).

Unlike for CrN and TiN monolithic coatings, Ti/TiN multilayer exhibited a reduced intensity of cracks. SEM micrographs of Fig. 6(b) and (e) illustrate the significant difference in deformation mechanisms beneath the indenter between the monolithic and multilayered coating/Zr-based BMGs systems. Indeed, the mean length and cracks density

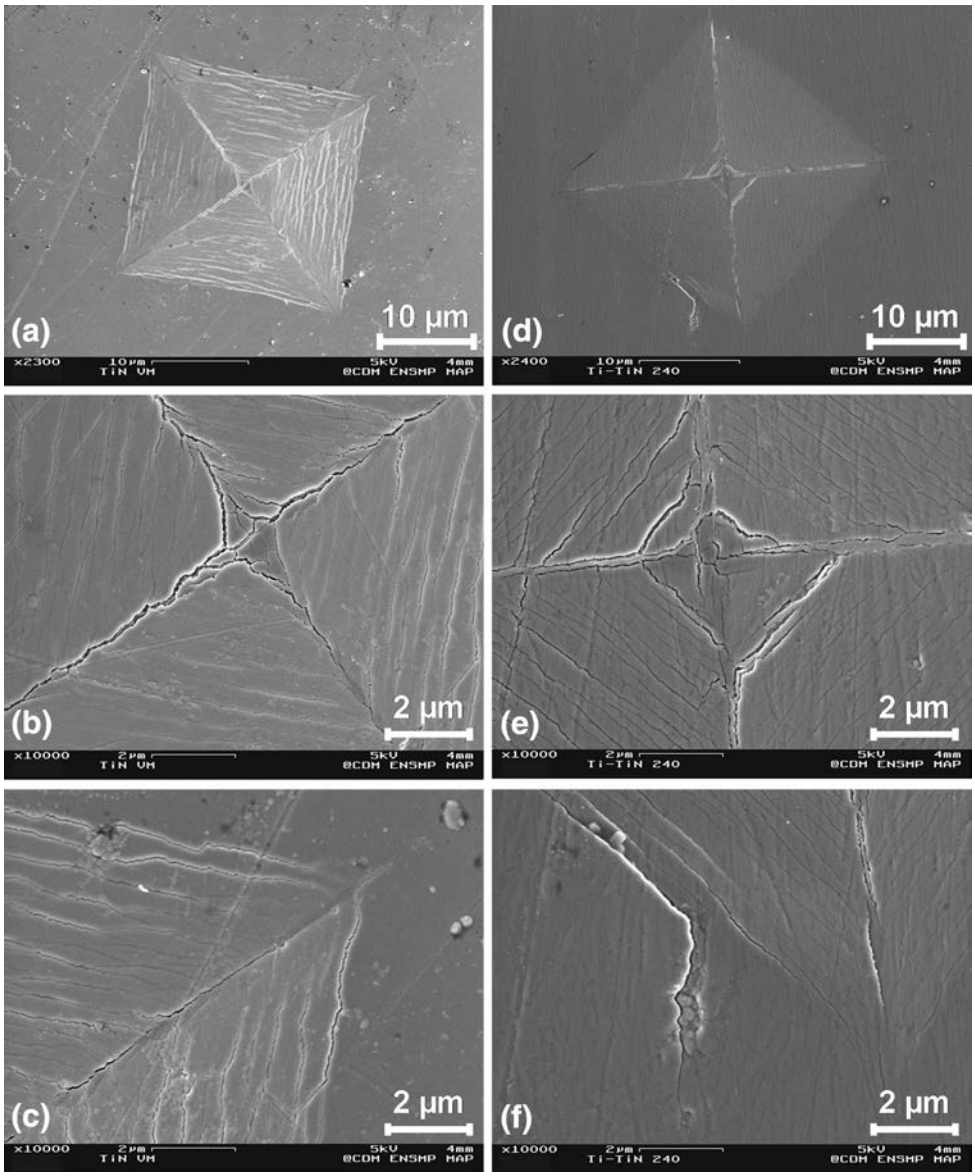

Fig. 6 SEM of imprints obtained after microindentation at an applied load of 3 N (a-b) TiN monolayer (c-d) Ti/TiN multilayers (e-f) shear bands in $Zr_{60}Ni_{10}Cu_{20}Al_{10}$.metallic glass

are higher in the case of the monolithic coatings. Further, evidence of shear band patterns is observed inside the impression of Zr60-based BMG using 3 N indentation load, as indicated by arrows on the SEM micrographs in Fig. 6(c) and (f).

3.2 Quantitative Analysis

Following the nanoindentation load-depth data, the H and E_r were determined; these quantities can be derived using the relations (Ref 19):

$$H = \frac{P}{A} \qquad \text{(Eq 1)}$$

$$S = \left.\frac{dP}{dh}\right|_{P\max} = 2\frac{E_r\sqrt{A}}{\sqrt{\pi}} \qquad \text{(Eq 2)}$$

where H is the hardness of the material being tested, P is the applied load, A is the projected contact area between the indenter and the specimen, S is the elastic constant stiffness defined as the slope of the upper portion of the unloading curve.

The composite modulus, E_r is given by

$$\frac{1}{E_r} = \left[\frac{1-\nu_i^2}{E_i}\ldots+\frac{1-\nu_s^2}{E_s}\right]^{-1} \qquad \text{(Eq 3)}$$

E_s and υ_s are Young's modulus and Poisson's ratio for the sample, and E_i and υ_i are Young's modulus and Poisson's ratio for the indenter.

The Eq 1 and 2 may be rearranged to yield:

$$\frac{H}{E_r^2} = \frac{4P}{\pi S^2} \qquad \text{(Eq 4)}$$

The parameter $\frac{H}{E_r^2}$ is independent of the projected area of the indent and is a measure of the material's resistance to plastic penetration. However, the dimensionless $\frac{H}{E_r}$ ratio shows similar

variation with number of cyclic loadings as the $\frac{H}{E_r^2}$ parameter and could be used to evaluate the deformation relative to yielding, as reported in (Ref 29, 30). The variation of $\frac{H}{E_r}$ ratio as function of number of cycle for different samples and from the integral of the load-displacement curves, we plotted also the W_p/W_t ratio of the dissipated energy during nanoindentation, where W_p is the plastic energy and W_t the total energy ($W_t = W_p + W_e$; W_e is the elastic energy), as shown in Fig. 7. Those parameters are an indication of the resistance to plastic deformation of the indented samples. Evidence of an increase of elastic recovery is from the plots of the variation of W_p/W_t ratio with the number of cycle. It is presumed that the decrease observed in the plastic energy dissipation might be caused by the fact that indentation induces activation of shear transformation zones in Zr-BMG (Fig. 7a). As the stress is increased, more STZs become active and connect to form shear bands in which heavy deformation leads to free volume creation (Ref 25). The competition between nucleation of shear bands increases inelastic deformation, and propagation of shear bands to sample surface induces a reduction of shear bands density which in turn leads to an increase of the elastic recovery ($1 - W_p/W_t$ ratio) (Ref 31). However, in the case of coatings, the plastic energy dissipation is significantly different. In fact, it is clearly illustrated that TiN presents the highest resistance to plastic deformation (almost no variation of the W_p/W_t ratio with the number of cycle as seen in Fig. 7b) compared to Ti/TiN multilayer (Fig. 7c) and the CrN monolithic (Fig. 7d) coatings.

Figure 8(a) shows typical nanoindentation curves of the tests performed on coated Zr-based metallic glasses with CrN, TiN monolayer, and Ti/TiN multilayer coatings at a maximum load of 3000 μN and a loading rate of 1000 μN/s. The mechanical properties and the elastic recovery parameter h_e/h_{max} with h_e which is the elastic depth and h_{max} the maximum indentation depth determined from load-displacement curves are listed in Table 2. The advantage of using h_e/h_{max} ratio is that it can be directly obtained from the unloading curve and is very sensitive to any change in the real contact area caused by the existence of residual stresses (Ref 32). It is worth noting that the h_e/h_{max} ratio of CrN and Ti/TiN is an indication of compressive residual stresses in the coatings.

In order to achieve accurate predictions of the distribution of the shear stress as a function of the indentation depth beneath the indenter, Bhowmick description based on the expanding cavity model for elasto-plastic flow of the film-substrate system was used (Ref 33).In this analysis, the load-displacement response of the system does not reflect deformation by dislocation movement, but shear-fracture stress dominates the plastic flow. Similar inter-columnar shear fracture in TiN films on ductile substrates has been reported by Ma et al. (Ref 34, 35) from observations of an indented zone made by a Vickers indenter.

The total indentation load P supported by the coated metallic glass system is assumed as the sum of the loads bearing capacity of coatings and substrates P_1 and P_2, respectively, with

$$\tau = \frac{P - P_2}{2\pi th \tan\theta} \quad \text{(Eq 5)}$$

$$P_2 = \frac{2\pi\sigma_S((h\tan\theta)^2 + 2ht)}{3}\left\{1 + Ln\left(\frac{1}{3}\frac{E_S\cot\theta}{\sigma_S}\right)\right\} \quad \text{(Eq 6)}$$

t is the total thickness of the deposited coating. The contact radius between indenter and material is $h \tan\theta$, where h is

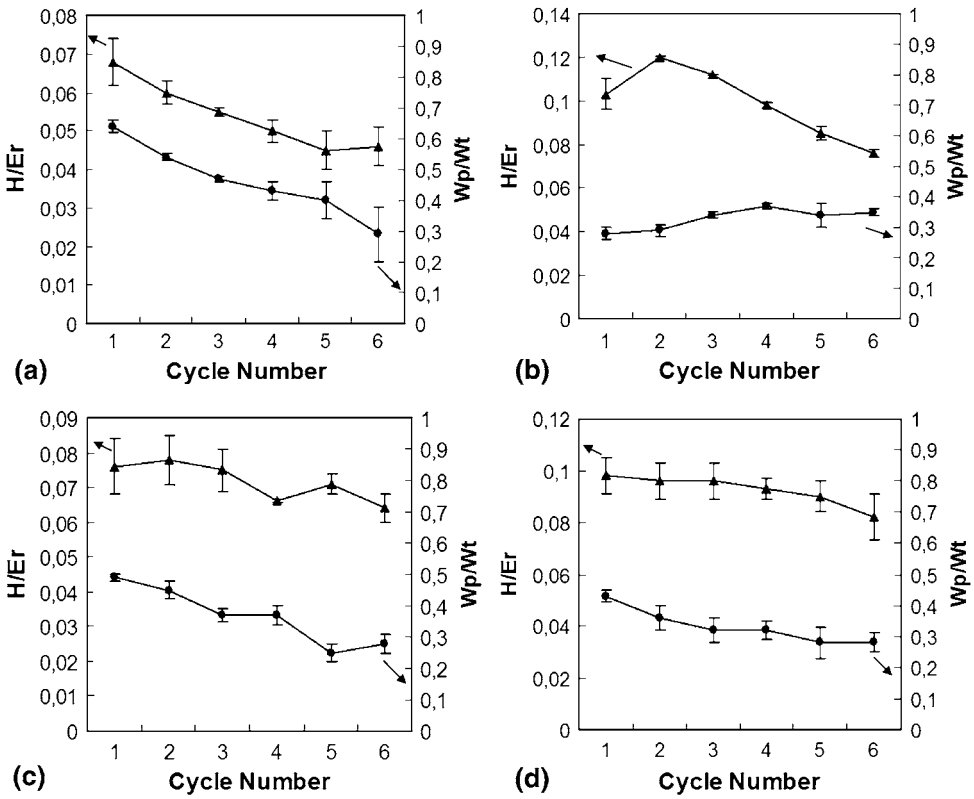

Fig. 7 Evolution of H/E_r and W_p/W_t for (a) Zr60-based BMG (b) TiN coated Zr60-based BMG (c) Ti/TiN coated Zr60-based BMG (d) CrN coated Zr50-based BMG obtained from cyclic nanoindentation tests at loading rates of 500 μN/s

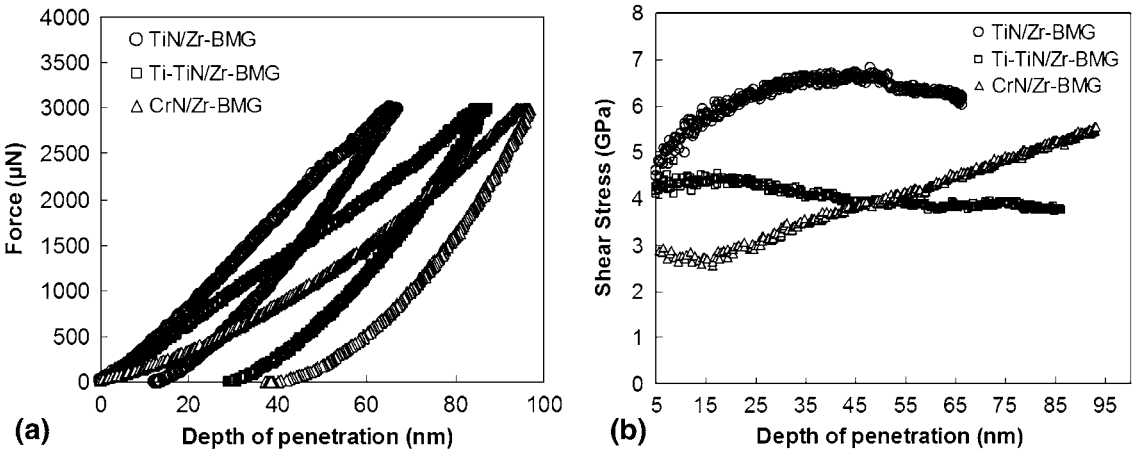

Fig. 8 Load-displacement profiles (a) TiN, CrN and Ti/TiN multilayer coated Zr-BMG obtained at 500 μN/s loading rate (b) Correspondant evolution of shear stress vs penetration depth

Table 2 Coatings properties obtained from conventional nanoindentation tests

Films/substrate systems	H (GPa)	E (GPa)	h_c/h_{max}
TiN/Zr60-based BMG	26.27	244.9	0.19
Ti-TiN/Zr60-based BMG	11.73	134.8	0.34
CrN/Zr50-based BMG	13.18	169.9	0.39

the indentation depth. P_2 is the load supported by the substrate, where σ_S is the yield stress and E_S is the Young modulus of the metallic glass substrate.

Substituting $E_S = 100$ GPa, $\theta = 70.3°$, $\sigma_S = 1.9$ GPa in Eq. 2 above, the shear stress is plotted as a function of the indentation depth during nanoindentation tests for monolithic TiN, CrN and Ti/TiN multilayer coatings, as observed in Fig. 8(b). These curves illustrate the decrease of shear stress when using a Ti/TiN multilayer coating comparing with the TiN and CrN ones. It is worth noticing the dependence of the shear stress on the nature of coatings, i.e., monolithic or multilayer.

The results described above can be explained by the fact that shear sliding characterizing the deformation behavior of monolayer coatings was reduced with the presence of Ti interlayer within a multilayer TiN structure. The application of Ti/TiN multilayer structure provided better resistance to plastic deformation and transgranular fracture compared to monolithic coatings. Those results are comparable with those finding by Xie et al. (Ref 36).

All the superior properties make Ti/TiN multilayer to be an effective protection coating for the enhanced fatigue strength of the bulk metallic glass substrates.

4. Finite Element Modeling

The experimental nanoindentation tests of monolayers CrN, TiN, and Ti/TiN multilayer nanocoatings were modeled by the finite element method (FEM) using commercial finite element code ABAQUS 6.10-1. Due to the axial symmetry of the problem, both the specimen and the indenter were modeled in two-dimensional axisymmetric in order to reduce computational time without compromising the accuracy. In FEM analysis, the indenter is modeled as an analytical rigid with a half-angle of 70.3° and thus has the same projected area-depth function as the standard Berkovich indenter.

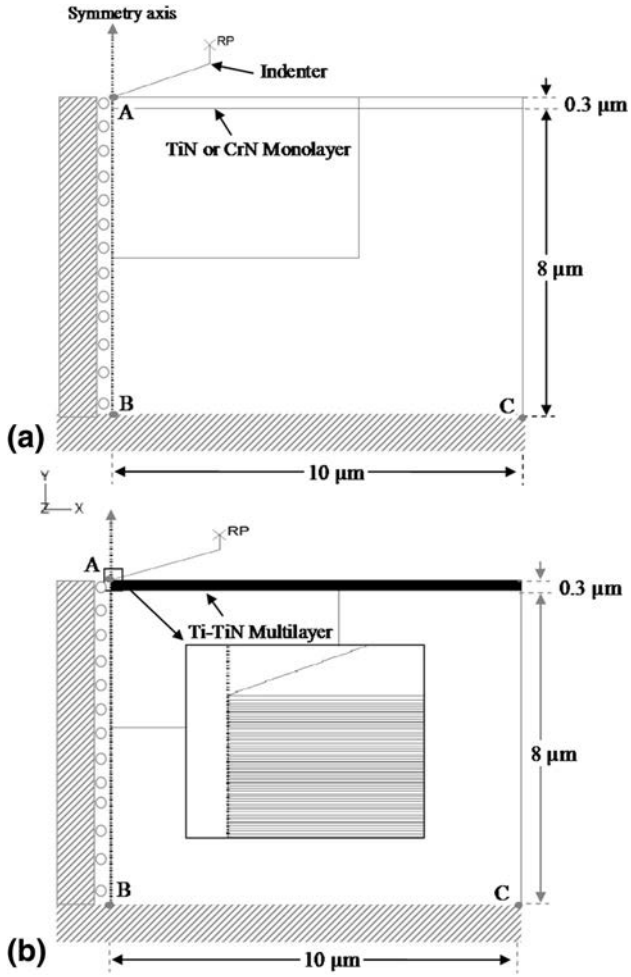

Fig. 9 Finite element models geometry and boundary conditions of (a) monolithic TiN and CrN (b) Ti/TiN multilayer coatings with details close to the region of contact

The contact between the rigid indenter and the specimen is assumed as frictionless. The finite element model for the specimen, illustrated in Fig. 9, was 10 μm in length and 8 μm in width. The thickness for the monolithic and multilayer is 300 nm. The interfaces between different layers were assumed to be perfectly bonded. The simulations are carried out under displacement-controlled conditions.

The two models of monolithic and multilayer coatings and the boundary conditions used for the simulation are schematically reported in Fig. 9. Roller boundary conditions are applied along the axis of symmetry, and the fixed boundary conditions are applied to the substrate base. Fine finite elements' mesh is used in the vicinity of the contact region for accurate analysis of the stress fields. The refinements were performed to ensure the results reported below, and based on the sensitivity analysis, it can be concluded that the simulation results have converged with respect to the mesh spacing for the benchmark mesh size and the model size used. The element mesh consists of four node bilinear axisymmetric quadrilateral elements with reduced integration (CAX4R) and three node axisymmetrical triangles (CAX3). The triangles are used to coarsen the mesh for increased computational efficiency. The number of elements used for monolithic and multilayer coatings is 7234 and 43,829 elements, respectively.

Table 3 Mechanical properties of coatings used for finite element analysis

Materials	E (GPa)	υ	σ_e (GPa)
Ti	120	0.3	1
TiN	400	0.25	6
CrN	380	0.22	4

Three coatings are of concern, monolithic TiN and CrN, and multilayer Ti/TiN (consisting of alternating Ti and TiN). The mechanical properties of Zr-based bulk metallic glasses substrates, and the used coatings are summarized in Table 3 (Ref 37). The mechanical properties of $Zr_{60}Ni_{10}Cu_{20}Al_{10}$ and $Zr_{50}Cu_{40}Al_{10}$ bulk metallic glass substrates were E = 104 GPa and E = 110 GPa, respectively, with a Poisson ratio ν = 0.36 (Ref 38, 39).

FEM analysis was performed to determine the effect of type of coating on the shear stress and equivalent plastic deformation distributions in coating substrate systems during nanoindentation at the same applied displacement (150 nm). The shear stress evolution along the coating thickness determined from the finite element simulation shown in Fig. 10 illustrates a difference in shear stress distribution for all the modeled coatings. The shear stress is localized in the coating for TiN

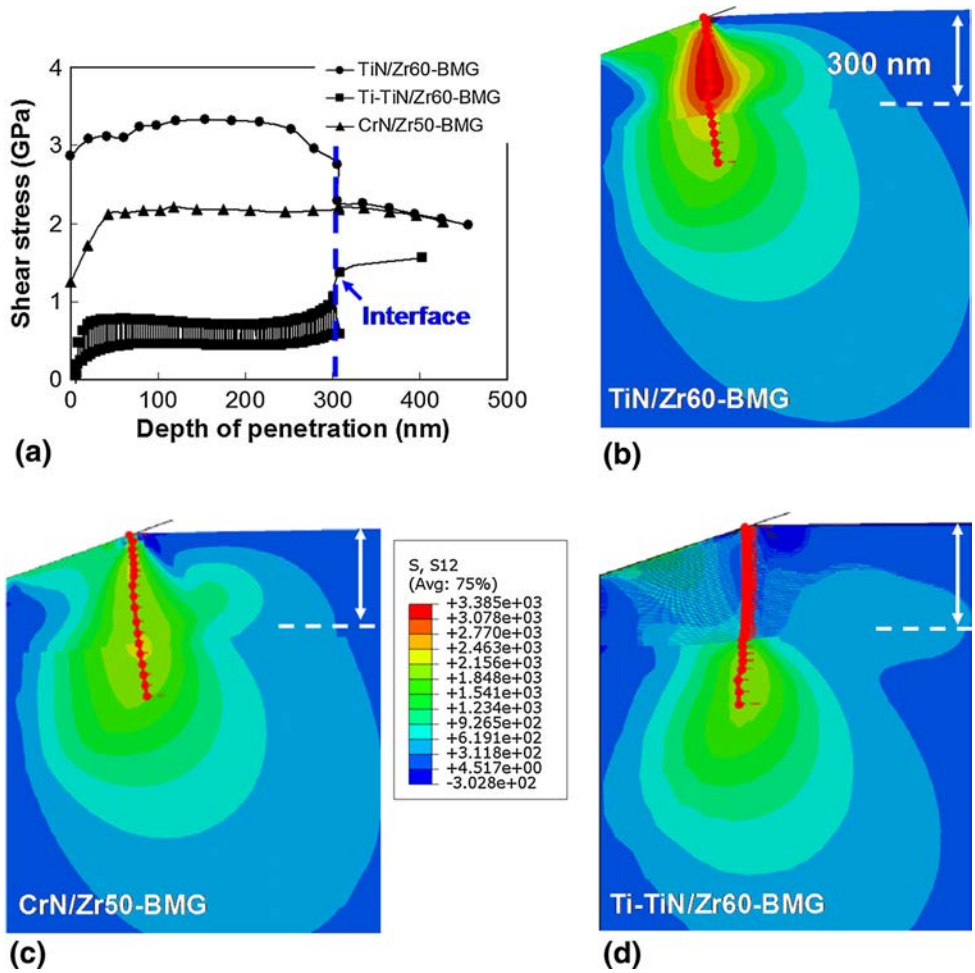

Fig. 10 (a) Shear stress variation along the vertical line for an applied displacement of 150 nm (b) TiN/Zr60-BMG system (c) CrN/Zr50-BMG system and (d) Ti-TiN /Zr60-BMG system

films, while the maximum shear stress distribution for CrN is located in film/substrate interface beneath the indenter. The lower values of shear stress are recorded for Ti/TiN multilayer coating. The results are in good agreement with the work of Voevodin et al. (Ref 40) indicating that the highest shear stress occurs under the substrate/coating interface, and this region may plastically deform causing adhesive and cohesive failure. Indeed, they showed that the normal and shear stresses in the substrate were reduced when using a multilayer coating. This is can be explained by the role of ductile Ti interlayer to decrease the shear stress and provides the highest energy absorption, by restricting cracks to individual layers and by distributing the damage throughout the multilayer system. Moreover, Huang et al. (Ref 41) reported that about 50% of the residual stress in the TiN film is relieved by the Ti interlayer.

Plastic deformation is considered as a major concern in the design and performance of engineering components. In fact, failure of hard coating can be caused by debonding of the coating from substrate (adhesive failure), or the large plastic flow in the subsurface (substrate failure), or the fracture of coating (Ref 38). Accordingly, it is imperative to determine the distribution of the plastic strain and the beginning of the plastic zone to have a better understanding of the mechanisms of surface and subsurface involving localized plastic flow.

Figure 11 shows the distribution of the plastic equivalent strain (PEEQ) at an applied displacement of 150 nm for the different studied systems. The PEEQ along the selected vertical path is significantly reduced to nearly zero at depth around 200 nm in Ti/TiN coating as revealed in Fig. 11(a). It can be seen that severe plastic strain is located in the coating immediately below the indenter. The localization of the equivalent plastic deformation in the deposited Ti/TiN multilayer coating can be referred to the role of ductile Ti interlayer absorbing the applied stress. Several studies show that multilayered Ti/TiN coatings display an improved fracture resistance as compared to TiN monolayer (Ref 42, 43), while for TiN and CrN monolayer films, the plastic deformation is initiated first in the surface beneath the indenter and then transmitted to the substrate at the interface. Furthermore, the value of transmitted equivalent plastic strain to the substrate in the case of TiN coating is higher than the corresponding value in CrN coating.

Figure 12 exhibits SEM tilted 34° view images of the cross section of residual indent for the TiN and Ti/TiN coatings obtained at an applied load of 10 N. The SEM view of the regular structure of the thin Ti/TiN multilayer achieved by the RF deposition technique (Fig. 12a) is compared with the swelling of the ductile Ti-layers as results of the accommodation of the plastic strain at the interfaces in the Ti/TiN-Zr BMG system as demonstrated in Fig. 12(b). The shear bands seen in the case of TiN monolithic coating beneath the indent show the load transfers to the substrate (Fig. 12c). These results agree well with the stress distribution predicted by FEM simulations

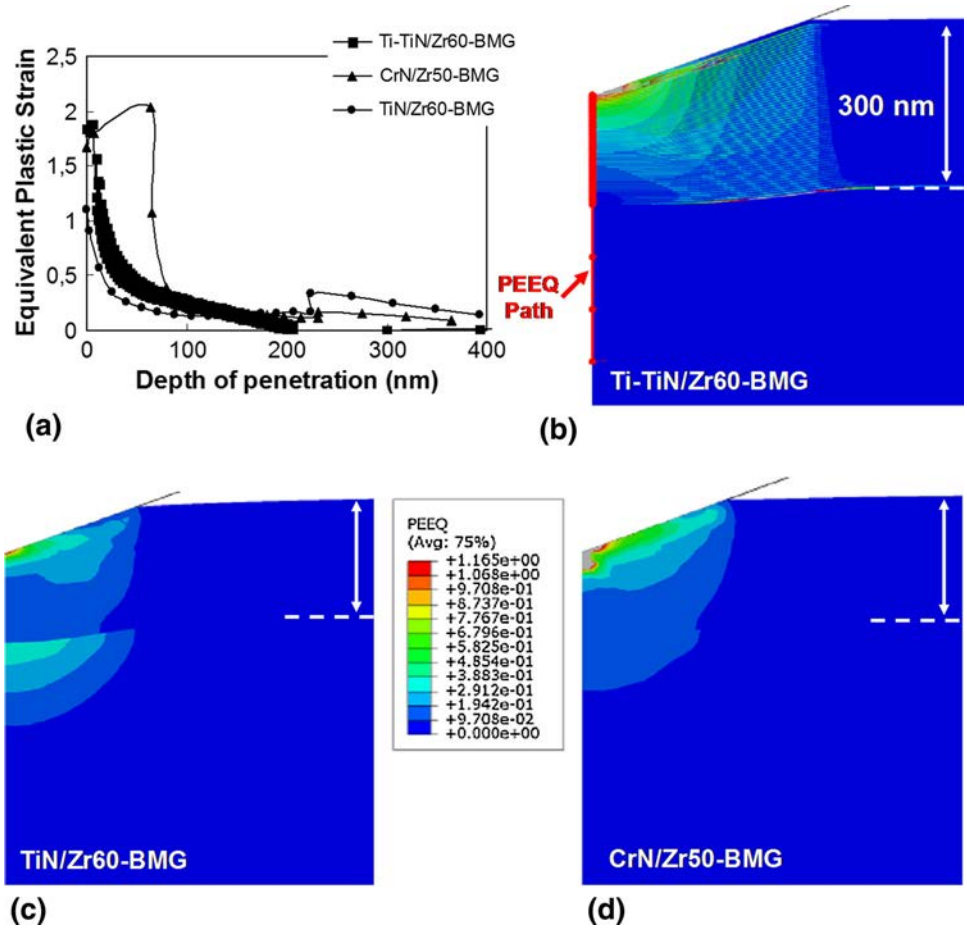

Fig. 11 (a) Plastic equivalent strain (PEEQ) variation along the vertical line and Contour plots of PEEQ in (b) TiN/Zr60-BMG system (c) CrN/Zr50-BMG system and (d) Ti-TiN /Zr60-BMG system

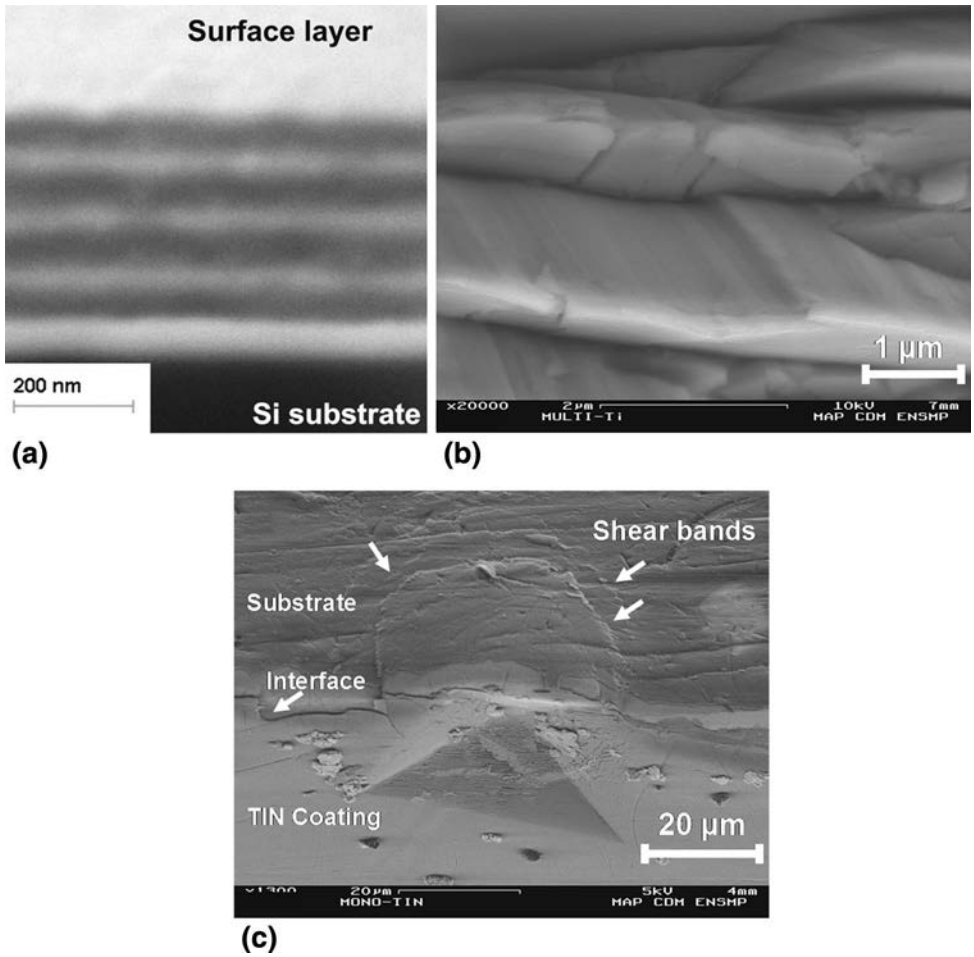

Fig. 12 SEM images of (a) Ti/TiN multilayer structure as deposited on Si substrate (b) Cross section of imprint obtained after Vickers indentation at a load of 10 N on Ti/TiN multilayer coated Zr60-based BMG (c) Tilted view 34° of the cross-section of residual indent after Vickers indentation at a load of 10 N on TiN coated Zr60-based BMG

(see Fig. 11), where the plastic strain distribution is localized in the multilayer thickness and transmitted to the substrate in the case of TiN and CrN monolithic coatings.

5. Discussion

In studying cyclic nanoindentation, our main concern is with unraveling the underlying physics of deformation mechanisms in TiN, CrN, Ti/TiN nanocoatings/Zr-BMG systems, and shear bands formation at interfaces. Do disparity and hysteresis loop details observed in the *P-h* curves are signal of discrete physical events beneath the indenter tip? Saraswati et al. (Ref 17) reported in calcium-doped gold, even in ppm levels such anomalous behaviors, which were related to dislocation activity. Indeed, when an indentation is produced, geometrically necessary dislocations (GD) were generated to form the permanent surface depression and play a key role in microplasticity. Increasing the depth of indentation increases the density of GD. However, during unloading, GD may reverse their slip partly, giving rise to a recovery microstrain that gets added to the elastic strain. The extent of reversible slip may appear as a softened behavior with a lower gradient to the reloading path than the unloading path of the previous cycle. Unlike for pure gold, hysteresis loops were observed in calcium-doped gold due to formation of Cottrell atmospheres on GD after unloading will make their slip more difficult on reloading. This could be manifested as hardening resulting in the reloading path having a higher gradient than the unloading path. In contrast to crystalline solids, in metallic glasses, there are no dislocations and grain boundaries, and the disparities observed at higher loads may not due to dislocation motion. Notwithstanding the small and confined volume of matter and for a given indentation load, the total number of shear bands formed to produce plastic flow most likely depends on random factors such as surface structure and orientation, statistical distribution, and orientation of STZs and the free volume forming the glass. Upon reloading, the stress-induced heat release of the deformed volume containing arrested bands may act as crack-like shear bands promoting the softening behavior, as illustrated in Fig. 6(c) and (d). Note that the disparity observed in *P-h* curves of the TiN films is not related to the extent of reversible slip but to formation of micro-cracks. Indeed, in situ SEM nanoindentation experiments clearly showed nucleation of radial cracks in TiN coating during loading and for higher loads adhesive and cohesive failure (Ref 44). Moreover, extensive investigation (Ref 33, 34) has shown that the columnar structure of TiN may not undergo plastic deformation under the indenter pressure but behaves like an

elastic medium and transfers the load to the substrate. Since the coating does not adjust to the deformation in the substrate, slip and column splitting occur outside the edge of the indentation.

The most obvious approach is the introduction of a ductile Ti interlayers in the TiN coatings (with a period thickness $\Lambda = 5$ nm) and subsequent changes of deformation mechanism. Hysteresis loops were produced as result of enhancing crack deflection along weak interlayer interfaces and exploiting the work hardening of the ductile phase (Ti). Indeed, it is argued that there are correlations between the hardness of a multilayered coating and the modulation period (Ref 45, 46). The enhancement in hardness for Ti/TiN was attributed to many interfaces that blocked the dislocation movement across interface layer due to differences in the shear modulus of the individual layer materials and by coherency strain causing periodical strain-stress fields in the case of lattice-mismatched multilayer films. In agreement with Caicedo et al. (Ref 47), the Ti/TiN multilayer produces a field stress that dissipates the applied load when the bilayer period is decreased.

However, both disparity and hysteresis loop are found in CrN-Zr50BMG system during cyclic nanoindentation. In fact, CrN films exhibited larger localized plasticity at the expense of lower yield stress compared to TiN coating. In agreement with Lee et al. (Ref 48), this result is attributed to the fact that CrN coating is softer than TiN coating as shown by nanoindentation tests (Fig. 8a). However, the size of the residual indentation does not simply reflect the overall plasticity of the system but a more complex combination of responses. These include elastic deformation, elastic flexure, and fracture of the coating as well as plastic yielding and fracture of the substrate. Load support by the coating reduces shear stresses and thus modifies the shape and size of the plastic zone as exhibited in Fig. 10 and 11.

Several previous numerical simulations have been used as an auxiliary tool to acquire better understanding of the indentation process. Indeed, Antunes et al. (Ref 49, 50) have reported 3D-numerical simulations of different film/substrate systems to study stress distributions. The FEM computational analysis used in this study confirms that Zr-BMG substrates act as a low yield stress plastic foundation, requiring the ceramic coating to flex elastically and plastically as the substrate deforms. Through thickness, cracking and interfacial fracture are possible. The exact mode of deformation depends not only on the mechanical properties of the coating and substrate, but also on the interface between the two, as demonstrated in Fig. 12. The stress distribution is transmitted to the substrate in the case of TiN and CrN monolayer (Fig. 12c). The accommodation of the stress at the interfaces between layers will be heterogeneous as evidenced by the swelling of the soft Ti-layers in Ti/TiN coating (see Fig.12b).

6. Conclusions

Cyclic nanoindentation is developed for fine-scale characterization of the effect of monolithic TiN, CrN, and Ti/TiN multilayer thin coatings on the mechanical performance and deformation mechanisms in the coating-Zr-based metallic glass systems. AFM, SEM observations, and FEM computational analysis were used, and the conclusions derived from the present work are listed below:

- Disparity event is found in load-displacement curves for Zr-based BMG and TiN-coated Zr60-based BMG and depends on the depth of penetration and loading rates. The disparity is attributed for Zr-based BMG and TiN film to crack-like shear bands and nucleation of micro-cracks, respectively.
- Hysteresis event is observed in Ti/TiN coating which is due to the enhancement of crack deflection along weak interlayer interfaces and work hardening of Ti ductile layers.
- Bhowmick model is employed to deduce the variation of shear stress with penetration depth. The shear stress values within the TiN and CrN monolithic coatings are higher than that found for the Ti/TiN multilayer coating.
- CrN and TiN films undergo a limited plastic deformation under the indenter pressure, behave like an elastic medium, and transfers the load to Zr-based BMG substrates.
- The FEM simulation and cyclic loading experiments demonstrate that the Ti/TiN coatings with soft Ti interlayer provide the highest energy absorption, by restricting cracks to individual layers and by reducing the stress field at film/substrate interface and which in turn can decrease the probability of shear band initiation on the metallic glass surface.

Acknowledgments

This work was supported by the French-Tunisian CMCU_Hubert Curien research program, Award no. 08G1122. The authors gratefully acknowledge Olek Maciejak for his technical assistance.

References

1. W.L. Johnson, Bulk Glass-Forming Metallic Alloys: Science and Technology, *Mat. Res. Bull.*, 1999, **24**(10), p 42–56
2. A. Inoue, B.L. Shen, H. Koshiba, H. Kato, and A.R. Yavari, Cobalt-Based Bulk Glassy Alloy with Ultrahigh Strength and Soft Magnetic Properties, *Nat. Mater.*, 2003, **2**, p 661–664
3. T.C. Hufnagel, P. El-Deiry, and R.P. Vinci, Development of Shear Band Structure during Deformation of a $Zr_{57}Ti_5Cu_{20}Ni_8Al_{10}$ Bulk Metallic Glass, *Script. Mater.*, 2000, **43**, p 1071–1076
4. C.C. Hays, C.P. Kim, and W.L. Johnson, Improved Mechanical Behaviour of Bulk Metallic Glasses Containing In Situ Formed Ductile Phase Dendrite Dispersions, *Mater. Sci. Eng. A*, 2001, **304–306**, p 650–655
5. S. Scudino, K.B. Surreddi, and J. Eckert, Mechanical Properties of Cold-Rolled $Zr_{60}Ti_5Ag_5Cu_{12.5}Ni_{10}Al_{7.5}$ Metallic Glass, *Phys. Status Solidi A*, 2010, **207**, p 1118–1121
6. M.H. Lee, K.S. Lee, J. Das, J. Thomas, U. Kühn, and J. Eckert, Improved Plasticity of Bulk Metallic Glasses Upon Cold Rolling, *Script. Mater.*, 2010, **62**, p 678–681
7. S. Scudino, B. Jerliu, K.B. Surreddi, U. Kühn, and J. Eckert, Effect of Cold Rolling on Compressive and Tensile Mechanical Properties of $Zr_{52.5}Ti_5Cu_{18}Ni_{14.5}Al_{10}$ Bulk Metallic Glass, *J. Alloy Compd.*, 2011, **S509**, p S128–S130
8. Y. Zhang, W.H. Wang, and A.L. Greer, Making Metallic Glasses Plastic by Control of Residual Stress, *Nat. Mater*, 2006, **5**, p 857–860
9. A.A. Voevodin, J.S. Zabinski, and C. Muratore, Recent Advances in Hard, Tough, and Low Friction Nanocomposite Coatings, *Tsinghua Sci. Technol.*, 2005, **10**, p 665–679
10. M. Kot, T. Moskalewicz, B. Wendler, W. Rakowski, and A. Czyrska, Micromechanical and Tribological Properties of nc-TiC/a-C Nanocomposite Coatings, *Solid State Phenom.*, 2011, **177**, p 36–46
11. S.-B. Qiu and K.-G. Yao, Novel Application of the Eletrodeposition on Bulk Metallic Glasses, *Appl. Surf. Sci.*, 2008, **255**, p 3454–3458

12. F.X. Qin, X.M. Wang, and A. Inoue, Observation of Bone-Like Apatite on Ti-Coated $Zr_{55}Al_{10}Ni_5Cu_{30}$ Bulk Metallic Glass After Alkali Treatment, *Intermetallics*, 2008, **16**, p 917–922
13. F.X. Qin, X.M. Wang, T. Wada, G.Q. Xie, K. Asami, and A. Inoue, Formation of Hydroxyapatite on Ti-Coated Ti-Zr-Cu-Pd Bulk Metallic Glass, *Mater. Trans.*, 2009, **50**(3), p 605–609
14. A. Tekaya, S. Labdi, T. Benameur, A. Piatkowska, P. Aubert, and J. Jagielski, Synthesis and Optimization of Ti–TiN Multilayered Protective Nanocoatings on Zr-Based Bulk Metallic Glass, *Surf. Coat. Technol.*, 2011, **205**, p 3404
15. A. Tekaya, T. Benameur, S. Labdi, and P. Aubert, Effect of Ti/TiN Multilayer Protective Nanocoatings on Zr-Based Metallic Glasses, *Thin Solid Films*, 2013, **539**, p 215–221
16. S.N. Dub, Y.V. Milman, D.V. Lotsko, and A.N. Belous, The Anomalous Behavior of Al-Cu-Fe Quasicrystal During Nanoindentation, *J. Mater. Sci. Lett.*, 2001, **20**, p 1043
17. T. Saraswati, T. Sritharan, S. Mhaisalkar, C.D. Breach, and F. Wulff, Cyclic Loading as an Extended Nanoindentation Technique, *Mater. Sci. Eng. A*, 2006, **423**, p 14–18
18. J.M. Antunes, A. Cavaleiro, L.F. Menezes, M.I. Simões, and J.V. Fernandes, Ultra-Microhardness Testing Procedure with Vickers Indenter, *Surf. Coat. Technol.*, 2002, **149**, p 27–35
19. C. Schuh, Nanoindentation Studies of Materials, *Mater Today*, 2006, **9**(5), p 32–40
20. W.C. Oliver and G.M. Pharr, An Improved Technique for Determining Hardness and Elastic Modulus Using Load and Displacement Sensing Indentation Experiments, *J. Mater. Res.*, 1992, **7**(6), p 1564–1583
21. C.A. Schuh and T.G. Nieh, A Nanoindentation Study of Serrated Flow in Bulk Metallic Glasses, *Acta Mater.*, 2003, **51**, p 87–99
22. A.S. Argon, Plastic Deformation in Metallic Glasses, *Acta Metall.*, 1979, **27**, p 47–58
23. C.A. Schuh and A.C. Lund, Atomistic Basis for the Plastic Yield Criterion of Metallic Glass, *Nat. Mater.*, 2003, **2**, p 449–452
24. F. Spaepen, A Microscopic Mechanism for Steady State Inhomogeneous Flow in Metallic Glasses, *Acta Metall.*, 1977, **25**, p 407–415
25. H.W. Sheng, W.K. Luo, F.M. Alamgir, J.M. Bai, and E. Ma, Atomistic Packing and Short-to-Medium-Range Order in Metallic glasses, *Nature*, 2006, **439**, p 419–425
26. K. Hajlaoui, T. Benameur, G. Vaughan, and A.R. Yavari, Thermal Expansion and Indentation-Induced Free Volume in Zr-Based Metallic Glasses Measured by Real-Time Diffraction Using Synchrotron Radiation, *Script. Mater.*, 2004, **51**(9), p 843–848
27. J.J. Lewandowski and A.L. Greer, Temperature Rise at Shear Bands in Metallic Glasses, *Nat. Mater.*, 2005, **5**, p 15–18
28. J. Richter, Application of Vickers Indentation for Assessment of PVD TiN Coated New Non Ledeburitic High-Speed Steels, *Surf. Coat. Technol.*, 2003, **162**, p 119–130
29. C. Rebholz, A. Leyland, J.M. Schneider, A.A. Voevodin, and A. Mattews, Structure, Hardness and Mechanical Properties of Magnetron-Sputtered Titanium-Aluminium Boride Films, *Surf. Coat. Technol.*, 1999, **120–121**, p 412–417
30. J. Musil, F. Kunc, H. Zeman, and H. Polakova, Relationships Between Hardness, Young's Modulus and Elastic Recovery in Hard Nanocomposite Coatings, *Surf. Coat. Technol.*, 2002, **154**, p 304–313
31. A. Tekaya, S. Labdi, T. Benameur, and A. Jellad, Quasi-Static Cyclic Loadings Induced Inelastic Deformation in a Zr-Based Bulk Metallic Glass Under Nanoindentation, *J. Mater. Sci.*, 2009, **44**, p 4930
32. Z.-H. Xu and X. Li, Influence of Equi-Biaxial Residual Stress on Unloading Behaviour of Nanoindentation, *Acta Mater.*, 2005, **53**, p 1913–1919
33. S. Bhowmick, V. Jarayam, and S.K. Biswas, Deconvolution of Fracture Properties of TiN Films on Steels From Nanoindentation Load-Displacement Curves, *Acta Mater.*, 2005, **538**, p 2459–2467
34. K.J. Ma, A. Bloyce, and T. Bell, Examination of Mechanical Properties and Failure Mechanisms of TiN and Ti-TiN Multilayer Coatings, *Surf. Coat. Technol.*, 1995, **76–77**, p 297
35. K.J. Ma, A. Bloyce, R.A. Andrievski, and G.V. Kalinnikov, Microstructural Response of Mono- and Multilayer Hard Coatings During Indentation Microhardness Testing, *Surf. Coat. Technol.*, 1997, **94–95**, p 322
36. Z.H. Xie, M. Hoffman, P. Munroe, and R. Singh, Microstructural Response of TiN Monolithic and Multilayer Coatings During Microscratch Testing, *J. Mater. Res.*, 2007, **22**(8), p 2312–2318
37. R.D. Conner, R.B. Dandliker, and W.L. Johnson, Mechanical Properties of Tungsten and Steel Fiber Reinforced $Zr_{41.25}T_{13.75}Cu_{12.5}Ni_{10}Be_{22.5}$ Metallic Glass Matrix Composites, *Acta Mater.*, 1998, **46**(17), p 6089–6102
38. Y. Sun, A. Bloyce, and T. Bell, Finite Element Analysis of Plastic Deformation of Various TiN Coating/Substrate Systems Under Normal Contact with a Rigid Sphere, *Thin Solid Films*, 1995, **271**, p 122–131
39. A.M. Dias, Numerical Study of Spherical Indentation in Superficial Coatings, *Int. J. Res. Rev. Appl.*, 2012, **11**(2), p 271–278
40. A.A. Voevodin, E.V. Iarve, W. Ragland, J.S. Zabinski, and S. Donaldson, Stress Analysis and In-Situ Fracture Observation of Wear Protective Multilayer Coatings, *Surf. Coat. Technol.*, 2001, **148**, p 38–45
41. J.-H. Huang, C.-H. Ma, and H. Chen, Effect of Ti Interlayer on the Residual Stress and Texture Development of TiN Thin Films Deposited by Unbalanced Magnetron Sputtering, *Surf. Coat. Technol.*, 2006, **201**, p 3199–3204
42. M.Y. He, F.E. Heredia, D.J. Wissuchek, M.C. Shaw, and A.G. Evans, *Acta Metall. Mater.*, 1993, **41**(4), p 1223–1228
43. E. Bemporad, M. Sebastiani, C. Pecchio, and S. De Rossi, High Thickness Ti/TiN Multilayer Thin coatings for Wear Resistant Applications, *Surf. Coat. Technol.*, 2006, **201**, p 2155–2165
44. K. Rzepiejewska-Malyska, M. Parlinska-Wojtan, K. Wasmer, and K. Hejduk, In-Situ SEM Indentation Studies of the Deformation Mechanisms in TiN,CrN and TiN/CrN, *Micron*, 2009, **40**, p 22–27
45. B. Borawski, J. Todd, J. Singh, and D.E. Wolfe, The Influence of Ductile Interlayer Material on the Particle Erosion Resistance of Multilayered TiN Coatings, *Wear*, 2011, **271**, p 2890–2898
46. J. Stallard, S. Poulat, and D.G. Teer, The Study of the Adhesion of a TiN Coating on Steel and Titanium Alloy Substrates Using a Multi-Mode Scratch Tester, *Tribol. Int.*, 2006, **39**, p 159–166
47. J.C. Caicedo, C. Amaya, L. Yate, O. Nos, M.E. Gomez, and P. Prieto, Hard Coating Performance Enhancement by Using $[Ti/TiN]_n$, $[Zr/ZrN]_n$ and $[TiN/ZrN]_n$ Multilayer System, *Mater. Sci. Eng. B*, 2010, **171**, p 56–61
48. S.Y. Lee, G.S. Kim, and J.H. Hahn, Effect of the Cr Content on the Mechanical Properties of Nanostructured TiN/CrN Coatings, *Surf. Coat. Technol.*, 2004, **177–178**, p 426–433
49. J.M. Antunes, L.F. Menezes, and J.V. Fernandes, Three-Dimensional Numerical Simulation of Vickers Indentation Tests, *Int. J. Solids Struct.*, 2006, **43**(3–4), p 784–806
50. J.M. Antunes, J.V. Fernandes, N.A. Sakharova, M.C. Oliveira, and L.F. Menezes, On the Determination of the Young's Modulus of Thin Films Using Indentation Tests, *Int. J. Solids Struct.*, 2007, **44**, p 8313–8334